THE JOURNAL OF PHYSICAL CHEMISTRY C
A JOURNAL OF THE AMERICAN CHEMICAL SOCIETY

pubs.acs.org/JPCC
Article

Photoelectrochemical Hydrogen Production from Surfactant-Rich Wastewaters: Proof-of-Concept and Mechanisms Investigation

Alessandro Chesini, Silvia Grandi,* Stefano Caramori, Michele Mazzanti, Luca Matteo Martini, Khakemin Khan, Michele Orlandi,* and Antonio Miotello

Cite This: J. Phys. Chem. C 2025, 129, 13860−13874

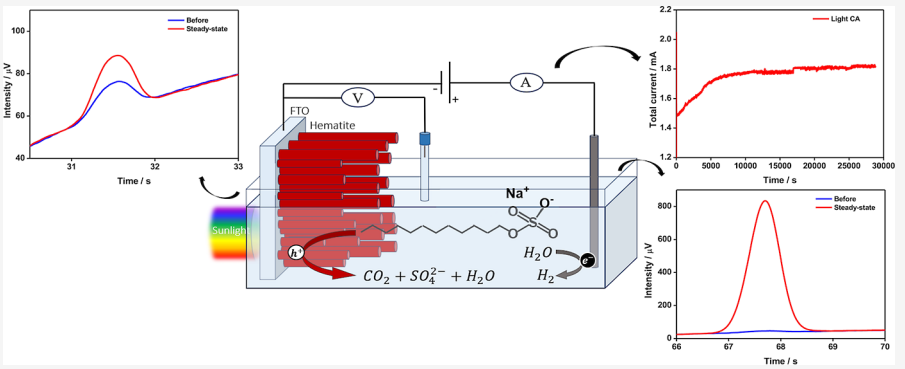

ABSTRACT: Solar hydrogen production currently employs pure water to prevent side reactions and damage to materials. Nevertheless, pure water is an increasingly valuable resource, and alternative substrates are required. In this work, we investigated a strategy for photoelectrochemical (PEC) solar hydrogen production from surfactant-rich wastewater. Sodium dodecyl sulfate (SDS) was used as a test-surfactant because of (1) its large use in industrial and domestic applications and consequently relevant concentration in wastewaters and (2) its potential suitability as a hole scavenger to enhance H_2 production. The working electrode of the PEC cell was a Ti-doped hematite photoanode, fully characterized to obtain information about crystallinity, morphology, and optical properties. Ongoing mineralization of SDS at the photoanode was characterized by the Gas Chromatographic (GC) detection of CO_2, with a radical-mediated oxidation mechanism revealed by fluorescence-based methods and Electrochemical Impedance Spectroscopy (EIS). H_2 production with simultaneous SDS oxidation and oxygen evolution, at 2.15 V RHE applied voltage, was quantified by GC. With a 1 cm^2 electrode, the production rate was 4.6 ± 0.3 μmol/h with a power saving efficiency (η, with respect to dark conditions) of 0.3%. A scale-up to 16.8 cm^2 area resulted in 22 ± 2 μmol/h with a η of 0.13%. These results provide a proof-of-concept for the valorization of surfactant-rich wastewaters as solar H_2 substrates.

1. INTRODUCTION

Renewable energy sources, especially solar, are playing an increasingly key role in substituting for fossil fuels. As a matter of fact, at the end of 2023, the global solar capacity accounted for 37% of the total renewable energy capacity and showed the greatest increase with respect to the previous year among renewables.[1] However, solar energy, like most of the green energy sources, presents some issues, such as intermittence and seasonal dependence. To overcome this, energy accumulation systems are necessary. In such a way, the stored energy can be used as soon as the source lacks. Up to now, batteries have proved to be a viable solution for small-scale applications but are more difficult to use at a larger scale.[2,3] A possible solution is to couple solar energy with hydrogen production from water electrolysis (PV-EL). Hydrogen is considered one of the best alternatives to fossil fuels because of its high specific gravimetric energy density and versatility, which makes it suitable for applications which may not require strong modifications to current technologies and the existing energy grid.[3,4] Through water electrolysis, the excess of solar energy, producing electrical current, is stored into the chemical bonds of molecular hydrogen, which can then be used as a fuel to provide energy whenever the renewable source is missing, or as a chemical feedstock in those sectors that are still strongly fossil fuel dependent.[5,6] In this perspective, water splitting through electrolysis is one of the most studied ways to produce hydrogen, but the process has several limits, like difficult kinetics, due to the slow water oxidation process and the poor

Received: March 25, 2025
Revised: July 18, 2025
Accepted: July 18, 2025
Published: July 24, 2025

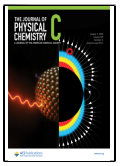

https://doi.org/10.1021/acs.jpcc.5c01995
J. Phys. Chem. C 2025, 129, 13860−13874

Scheme 1. Schematic Illustration of a Three-Electrode Configuration PEC Cell for SDS Degradation and Hydrogen Production

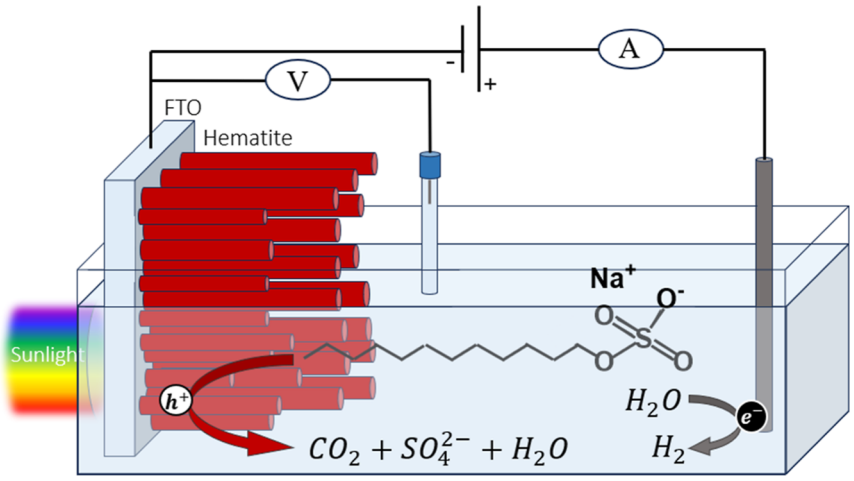

scalability of benchmark materials. These limits make the process quite expensive and difficult to scale up. Photoelectrochemical cells (PEC), which are partially or completely powered by sunlight, are a promising technology to tackle these issues, showing good results while using low-cost materials.[7−9]

In view of a large-scale application of either the PV-EL or the PEC technology, a further problem to consider is the conflict-of-use of freshwater. In fact, freshwater is projected to become an increasingly important resource, vital to sectors ranging from agriculture to industry and domestic use. To avoid this, an emerging idea in the field is that of using alternative water sources for hydrogen production, such as seawater[10,11] or different kinds of wastewater. Among these, pharmaceutical-containing effluents have been considered for simultaneous water remediation and hydrogen production,[12,13] while attempts have been made to attain urea-oxidation assisted water electrolysis.[14,15] From the hydrogen production perspective, a common issue in several of these studies is the low concentration of the compounds from which, compared to water, the photoanode could more easily extract electrons to employ in cathodic hydrogen evolution. The low quantity of oxidizable target species does not allow a significant boost in hydrogen production compared to a contaminant-free electrolyte. In the case of pharmaceuticals in particular, where concentrations are generally in the ppm range or below,[16] the advanced photoelectrochemical oxidation process at semiconductor photoanodes is indeed very promising for water remediation but less so for hydrogen production.

Within this framework, an innovative strategy would be to use wastewaters containing high concentrations of substrates potentially suitable as hole scavengers to enhance hydrogen production, such as surfactant-rich wastewaters. Surfactants, as a contaminant class, are not as problematic as pharmaceuticals, as they are often biodegradable, but they can easily reach concentrations in the range of 1−100 g/L, thus representing an environmental issue as well.[17−19] For instance, such large concentrations are dangerous for living beings, and the biodegradation process would lead to uncontrolled bacterial growth;[20] thus, they require treatment with the associated costs. Surfactants are organic amphiphilic molecules having a hydrophilic head and a hydrophobic tail. They are mainly used as detergents in many different applications, from laundry to the oil and textile industries. The intensive use of these substances and the necessity for abatement also call for new and cost-effective treatments. Sodium Dodecyl Sulfate (SDS), in particular, is one of the most used and widespread surfactants and, hence, one of the most detected species in wastewaters.[21]

Given these premises, we propose here to use a PEC process combining water remediation through the anodic degradation of surfactants with cathodic hydrogen production. As a consequence, the valorization of a waste is achieved, where photoelectrochemical oxidation of organic surfactants is paralleled by the chemical storage of solar energy into hydrogen. This latter could be obtained at reduced overpotentials, given the favorable kinetic competition between the oxidation of the organics, now present at a significant concentration level, and the oxygen evolution reaction (OER) involving water molecules as electron donors. In particular, in this work, we demonstrate, at a proof-of-concept level, the possibility of using SDS-containing waters as a source of electrons for hydrogen production in a PEC setup in a neutral environment (Scheme 1 below). This is of key importance, as it allows us to go beyond the state-of-the-art in several ways: (1) the direct use of wastewater as an electrolytic solution, without adjusting the pH or adding any supporting electrolyte. (2) The high concentration of the pollutant in the solution, thanks to its high solubility, also enables prolonged operation of the photoelectrochemical cell. These features are uncommon in standard wastewater treatment applications, where the pollutant content is rather low. This makes the addition of an external electrolyte unavoidable to ensure the conductivity of the cell, whereas the overall operational time is obviously limited by the small amount of pollutant.[22−24] (3) The oxidation of the surfactant at the photoanode suppresses the competing OER, thus reducing the oxygen and hydrogen recombination rate and ideally making the compartmentalization unnecessary. Moreover, the OH radical generation by electrochemical means, which is the key for the mineralization of organics in aqueous solution, requires specialized electrodes endowed with an extremely large overpotential for oxygen evolution. These electrodes, like carbon-doped diamond electrodes, tin, and lead oxide, are either quite expensive (the first) or environmentally hazardous (the last) and generally suffer from conductivity

https://doi.org/10.1021/acs.jpcc.5c01995
J. Phys. Chem. C 2025, 129, 13860−13874

issues. Extremely large voltages are required for the operation of such electrodes, which are around 2 V vs NHE in concentrated sulfuric acid.[25] Thus, the observation that a visible absorbing photoanode made of cheap and environmentally benign materials such as Ti(IV)-doped hematite can stably operate under neutral conditions, even in diluted electrolyte conditions, and achieve mineralization of hydrocarbon chains is a step forward in the development of sustainable remediation processes coupled to hydrogen evolution.

In this work, the cell is set in a three-electrode configuration, with a Ti-doped α-hematite (Ti:α-Fe_2O_3) photoanode as the working electrode, a Pt counter electrode, and either a Ag/AgCl or SCE reference electrode. This modified hematite was chosen as semiconducting material because of its appealing properties, like stability in these operating conditions, earth-abundancy, and suitable band gap energy (2−2.2 eV), which allows a large portion of the solar spectrum to be harvested.[26] Since pure hematite as a photoanode also shows important issues, where sizable fractions of charge carriers exhibit short diffusion length ($L_h \approx 2-4$ nm) and fast recombination rates (in the order of ps),[27] we adopt here a Ti^{4+} doping strategy to enhance its performance.[8,27]

The Ti:α-Fe_2O_3 photoelectrode was synthesized following a hydrothermal procedure and was characterized through microRaman, UV−vis spectroscopy, scanning electron microscopy with energy dispersive X-ray analysis (SEM-EDXS), X-ray photoelectron spectroscopy (XPS), X-ray diffraction (XRD), and photoluminescence (PL) analysis, allowing us to elucidate the role of the Ti(IV) doping on the charge-separation process. The PEC cell is operated under AM 1.5 G illumination provided by a solar simulator (0.1 W/cm^2), while the electrochemical reaction mechanism is investigated through electrochemical impedance spectroscopy (EIS), IPCE, and a photoluminescence radical detection assay based on the coumarin/hydroxycoumarin conversion. Finally, SDS degradation and hydrogen production are investigated through gas chromatography (GC).

2. EXPERIMENTAL SECTION

2.1. Synthesis. Ti:α-Fe_2O_3 photoanodes were synthesized on a fluorine-doped SnO_2 (FTO) conductive glass following a hydrothermal approach as described elsewhere.[28] The FTO glass was cleaned through ultrasonication in isopropanol and then rinsed with deionized water. FTO glass substrates were first dip-coated in a solution containing an Fe(III) oleate precursor added with 15 mM Ti(IV) isopropoxide. The dip coating solution was prepared by adapting a literature procedure.[29] The resulting layer is then annealed at 500 °C for 30 min to convert the precursor into hematite. This layer is useful to promote the growth of a nanocrystalline film of FeOOH during the hydrothermal synthesis, which was carried out in a Teflon-lined stainless steel autoclave filled with an aqueous solution (95% H_2O and 5% ethanol v/v) containing a sodium salt (0.91 M $NaNO_3$) at a pH value of 1.5 adjusted with 6 M HCl, the iron precursor (0.136 M $FeCl_3 \cdot 6H_2O$), and a titanium dopant (2.5 mM Ti_2CN). The seed-layered electrodes were inserted into the Teflon liner, lying at an angle of ca. 45° with respect to the vertical liner walls, and heating at 95 °C was applied for 4 h. The obtained FeOOH yellowish films are rinsed with deionized water and then converted into Fe_2O_3 by sintering in air at 550 °C for 1 h. The resulting films were modified by a chemical bath treatment in a 0.2 M $TiCl_4$ solution heated at 50 °C to induce Ti doping, followed by a 10 min thermal activation at 760 °C, leading to the Ti:α-Fe_2O_3 electrodes used for this study. This final high-temperature treatment is a well-established and standardized procedure to induce tin atom migration from the FTO substrate to the hematite layer, increasing conductivity, and is considered essential for performance.[30] As this step has been applied to all electrodes produced here, inclusion of Sn is not explicitly indicated in sample labels.

α-Fe_2O_3 photoanodes without Ti doping were also produced for comparison, adapting the procedure described above.

2.2. Materials Characterization. Scanning Electron Microscopy (SEM) was used to characterize the morphologies of the working electrodes. The measurements were performed on a Field Emission SEM, JSM 7001 F JEOL, at a 30 keV electron beam energy. SEM was coupled with an EDXS detector (EDXS, Oxford INCA PentaFET-x3) for sample elemental composition analysis.

μ-Raman spectroscopy was used for composition and structural properties analysis (crystal phase and degree of crystallinity). The results were collected by a Micro-Raman configuration (Horiba LabAramis, 100× magnification), through a 633 nm He/Ne laser, an 800 L/mm grating, and a CCD detector.

UV−vis spectroscopy was performed in a Cary Varian 5000 UV−vis−NIR spectrophotometer. From the transmittance spectra, Tauc plots were used to evaluate the Ti:α-Fe_2O_3 band gap energy.

X-ray photoelectron spectroscopy (XPS) analysis, employing a monochromatic Al Kα (1486.6 eV) X-ray source, was conducted to examine the surface chemical states of the elements present in the sample. The binding energy values of all elements were calibrated using the C 1s peak at 284.8 eV as a reference.

The luminescence spectra were measured at room temperature by using an FLS920 emission spectrometer (375 nm excitation wavelength) (Edinburgh Instruments).

The crystalline structures of the as-synthesized materials were investigated by using a Bruker D8 Advance X-ray diffractometer equipped with Cu Kα radiation (λ = 0.154 nm).

2.3. Electrochemical and Photoelectrochemical Methods. Electrochemical experiments were run in a quartz tube reactor, filled with 170 mL of 1 g/L SDS (3.5×10^{-3} M) water solution. Cyclic Voltammetry (CV), Linear Sweep Voltammetry (LSV), and Chronoamperometry (CA) were acquired through a Gamry Interface 1000 potentiostat, in a three-electrode configuration using a Pt mesh and Ag/AgCl or SCE as a counter and reference electrode, respectively. All the measured potentials were then converted to RHE by means of the Nernst equation

$$V_{RHE} = V_{Ag/AgCl} + 0.200\ V + 0.059 \times pH \quad (1)$$

$$V_{RHE} = V_{SCE} + 0.241\ V + 0.059 \times pH \quad (2)$$

CVs were run at 50 mV/s with a 5 mV step, while LSV were run at either 5 or 20 mV/s with steps of 5 mV. CA was performed by applying a constant potential of 2.15 V vs RHE.

The quartz tube was closed with an airtight Teflon cap and electrode support. The illumination was provided by a solar simulator, a Quantum Design LS0306, with a 300 W Xe lamp coupled with an AM 1.5 G filter. The irradiated power was 1 sun (100 mW/cm^2) on a circular spot with a diameter of 4 cm.

https://doi.org/10.1021/acs.jpcc.5c01995
J. Phys. Chem. C 2025, 129, 13860−13874

All of the experiments were carried out in a Faraday cage to screen external electromagnetic noise.

To investigate the performance in electron−hole generation of the Ti:α-Fe_2O_3 electrodes, Incident Photon to Current Efficiency (IPCE) experiments were carried out. The PEC was set in a three-electrode configuration, with a Ti:α-Fe_2O_3 photoanode as a working electrode, a Standard Calomel Electrode (SCE) as a reference electrode, and a Pt wire as a counter electrode. We performed the measurements using an aqueous solution containing 1 g/L SDS, applying an external bias of 2.0 V vs RHE, which was provided by an Amel model 552 potentiostat. A 150 W Luxtel xenon lamp coupled with an Applied Photophysics LTD monochromator set at a 10 nm passband supplied the illumination. The incident radiant power was referenced to a calibrated photodiode. The photoconversion efficiency was collected in the hematite absorption region, between 340 and 600 nm.

EIS under simulated sunlight illumination (ABET AM 1.5 G, 0.1 W/cm^2) was recorded in various aqueous electrolytes: 3.5 × 10^{-3} M $NaClO_4$ (el 1), 3.5 × 10^{-3} M SDS (el 2), 3.5 × 10^{-3} M $NaClO_4$ + 3.5 × 10^{-3} M MeOH (el 3), or 3.5 × 10^{-3} M $NaClO_4$ + 3.5 × 10^{-3} M SDS (el 4). In all cases, the pH was adjusted to pH 7 with either NaOH or $HClO_4$. We note that 3.5 × 10^{-3} M corresponds to 1 g/L SDS. Thus, comparable concentrations of electron-donating sacrificial species (either SDS or MeOH) and supporting electrolytes are present in the formulations above. We note that SDS behaves both as a possible hole scavenger and a supporting electrolyte; thus, for comparative reasons, we have used the same concentration of $NaClO_4$ as an "inert" supporting electrolyte. EIS was obtained with a 10 mV sinusoidal perturbation within the frequency range of 20,000−0.05 Hz by sampling the J/V characteristic of working electrodes in each of the electrolytes specified above at intervals of ca. 130 mV in the voltage range 1.1−2.0 V vs RHE. Data acquisition was accomplished with a PGSTAT 302/N equipped with an FRA2 Frequency Response Analyzer. Control J/V curves recorded at the beginning and at the end of each multivoltage EIS acquisition showed a substantial stability of the photoelectrodes during these experiments. Fitting of EIS data was achieved in terms of equivalent circuit with Zview.

The circuits in Scheme 2 below were adopted, consistent with nested electrical models often used to describe the impedance response of hematite.[31−33] Here, the parallel R_{rec}/C_{ss} represents the charge transfer resistance of the photoelectrode, and R_{ct}/C_{sc} represents the transport across the space charge layer. As shown in Figure S11, several Nyquist plots at different potentials show a 45° slope at high frequencies; this experimental feature can be well reproduced by adding a short Warburg element (W_S) to our equivalent circuit, that, according to Taylor and Gileadi, may arise from mass transport limitations due to slow diffusion of electrolyte species within the mesoporous semiconductor, that would lead to an additional resistance in series.[34]

The Warburg element (W_S) models the diffusional resistance of the electrolyte within the pores of the mesoporous semiconductor, which, in the conditions herein adopted, is significant given the low electrolyte concentration compared to what is more commonly reported in photoelectrochemical applications oriented toward energy conversion (molar or decimolar electrolyte concentration).[35]

2.4. General Analytical Methods. Optical emission measurements were performed with an Edinburgh Instrument FLS920, equipped with a double emission monochromator, a 900 W arc Xenon lamp, and a photomultiplier tube (PMT, Hamamatsu R928P) as the detector for UV−visible wavelengths.

Scheme 2. Equivalent Circuit Used to Fit EIS Data under Illumination

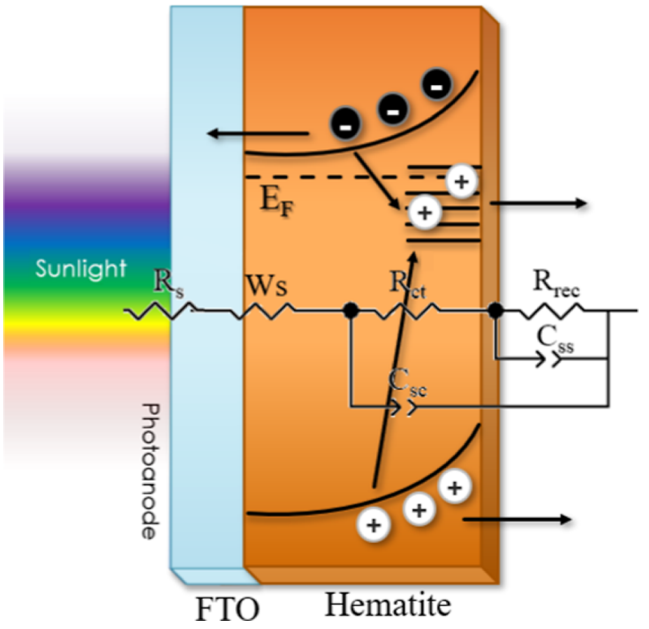

To perform coumarin fluorescence experiments, 10^{-4} M coumarin was added to 1 g/L of SDS aqueous solution. These measurements were performed by exciting the sample solution at 332 nm (2 nm band-pass), which is the maximum absorption peak (λ_{max}) of coumarin, and recording the emission spectra between 350 and 600 nm (2 nm band-pass), where it is possible to observe the hydroxy-coumarin emission band. The fluorescence spectrum was acquired before and after 1 h at 1 sun (100 mW/cm^2) illumination of the Ti:α-Fe_2O_3 photoelectrode kept under polarization at 2.0 V vs RHE in a three-electrode configuration PEC cell using a Pt wire as a counter.

Gas chromatograms were acquired to assess the hydrogen (i.e., the amount of solar fuel) and carbon dioxide (i.e., the product of the degradation of the pollutant) contents produced by the cell. These experiments were run in an Agilent 990 Micro GC instrument equipped with a Molsieve 5 Å and a Plot-U column with argon as a carrier gas and a TCD detector. The reactor is constantly fluxed with a 10 sccm N_2 flow (99.999% purity). Effluents from the reactor were sampled inline by the GC.

The responsivity of GC for the analytes was determined from chromatograms obtained for known concentrations of the gas of interest in nitrogen mixtures. Different reference solutions were prepared through dynamic gas dilution admixing H_2 (99.999% purity) or CO_2 (99.998% purity) in N_2 (99.999% purity). In the actual experiments, at each moment of interest, the area of a given peak is calculated by averaging 5 consecutive acquisitions. The error on the estimated concentration of H_2 and CO_2 is around 7%, and it is mainly due to the accuracy in the determination of the responsivity of the GC (more details in the Supporting Information).

https://doi.org/10.1021/acs.jpcc.5c01995
J. Phys. Chem. C 2025, 129, 13860−13874

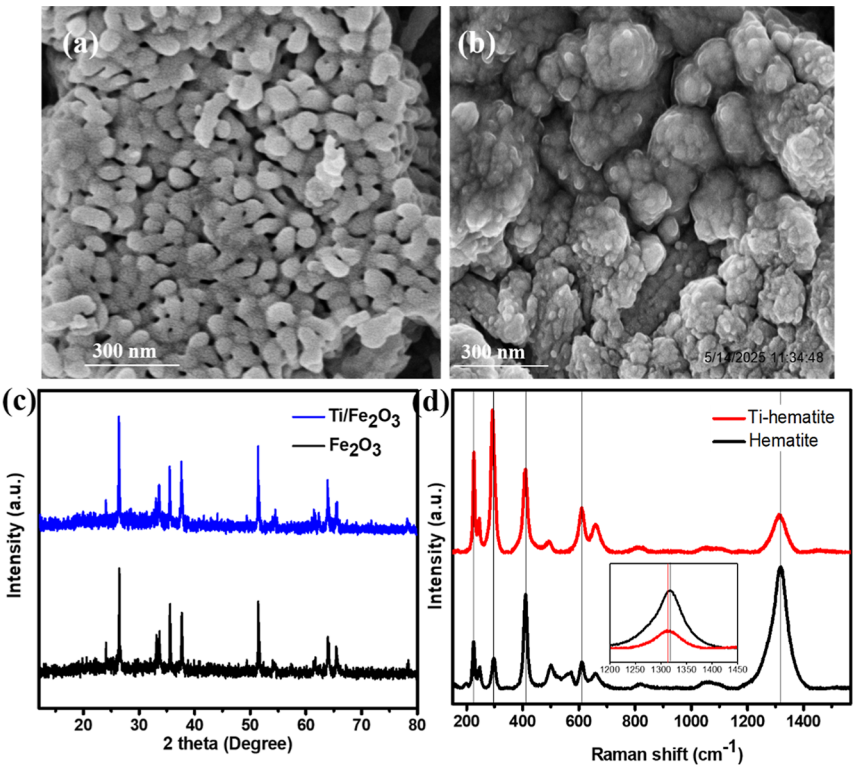

Figure 1. (a) SEM image of Fe_2O_3 (b) SEM image of Ti:α-Fe_2O_3 (c) XRD pattern of Fe_2O_3 and Ti:α-Fe_2O_3 (d) Raman spectra of Fe_2O_3 and Ti:α-Fe_2O_3.

3. RESULTS AND DISCUSSION

3.1. Ti:α-Fe_2O_3 Morphology and Composition. Figure 1 shows the SEM images of the as-prepared Fe_2O_3 and Ti:α-Fe_2O_3 electrodes. The deposition process creates a uniform film across the entire unmasked area. Interestingly, the undoped sample, when paired with a seed layer, exhibits a porous structure of vertically aligned nanorods sintered together, as can be seen in Figure 1a. The compact morphology is likely induced by the increased number of nucleation sites provided by the seed layer. This leads to a denser nanorod array compared to the typical morphology of hematite nanorods. Ti(IV) doping induces a change in morphology, as can be seen in Figure 1b, with more closely packed features. The crystal phase of the hematite thin film was studied by using XRD, where all the residual peaks, coming from the deposited iron oxide layer, can be indexed to the hematite hexagonal phase (JPCSD #33-0664), as shown in Figure 1c. The Ti doping was further investigated through the Raman spectroscopy technique. As shown in Figure 1d, all of the main peaks of the Ti(IV)-doped hematite are the same as the pristine hematite, except that the peaks in Ti(IV)-doped hematite are slightly shifted toward the left, indicating the successful incorporation of Ti(IV) into the crystal lattice of hematite. The presence of titanium was also confirmed through EDX, as shown in Figure S10.

The XPS spectrum for Ti:α-Fe_2O_3 is shown in Figure 2. The Fe $2p_{3/2}$ signal (a) is located at 708 eV, and the O 1s signal (b) is at 527 eV, indicating the presence of hematite.[36,37] Besides these, Ti(IV) is also revealed at a binding energy (B.E.) of 458.50 eV for the Ti $2p_{3/2}$ peak. As shown in Figure 2c. This value is slightly lower than the standard B.E. of TiO_2 (around 458.7 eV). This suggests that titanium within the Ti-doped α-Fe_2O_3 thin film likely exists in the form of TiO_2. The observed deviation in binding energy data could be due to a mutual chemical interaction between Fe_2O_3 and TiO_2 during the doping process.[38−41]

3.2. Unravelling the Impact of Ti on Charge Separation. UV−visible diffuse reflectance spectra of Fe_2O_3 and Ti:α-Fe_2O_3 were also collected to investigate the effect of Ti(IV) doping on the properties of the Fe_2O_3 electrode. As shown in Figure 3a, the absorption onset of Fe_2O_3 is located in the 550−580 nm range, and the corresponding band gaps of the pure sample were found in the 2−2.2 eV range depending on the preparation method. Interestingly, the Ti(IV)-doped samples show a gradual but steady decrease in the band gap, which could be the consequence of the formation of intraband gap states or of a mixed oxide phase. Besides the UV−visible diffuse reflectance spectra, the presence of Ti(IV) was also confirmed from the Raman peaks for the doped and pristine samples. In the Ti(IV) modified sample, the Raman peaks are slightly shifted, compatible with interstitial Ti(IV) doping in the lattice of Fe_2O_3, as shown in Figure 1d and discussed above. In order to investigate the effect of the Ti(IV) treatment on the photogenerated charge separation, a steady state photoluminescence (PL) spectrum of Fe_2O_3 and Ti:α-Fe_2O_3 is shown in Figure 3c. Both the Fe_2O_3 and Ti:α-Fe_2O_3 samples exhibit a broad emission band centered at 550 nm. The slight decrease of the intensity of PL spectra of Ti-doped Fe_2O_3 is consistent with the suppression of surface states where electrons can trap, thus reducing the yield of radiative recombination involving trapped carriers, which follows the formation of titanium-rich phases at the surface of the photoanode, comprising either mixed metal oxides (iron titanates) or a TiO_2 rutile-like phase depending on the local ratio of Ti(IV) and Fe(III). This is consistent with previous observations made on chemically related photoanodic

https://doi.org/10.1021/acs.jpcc.5c01995
J. Phys. Chem. C 2025, 129, 13860−13874

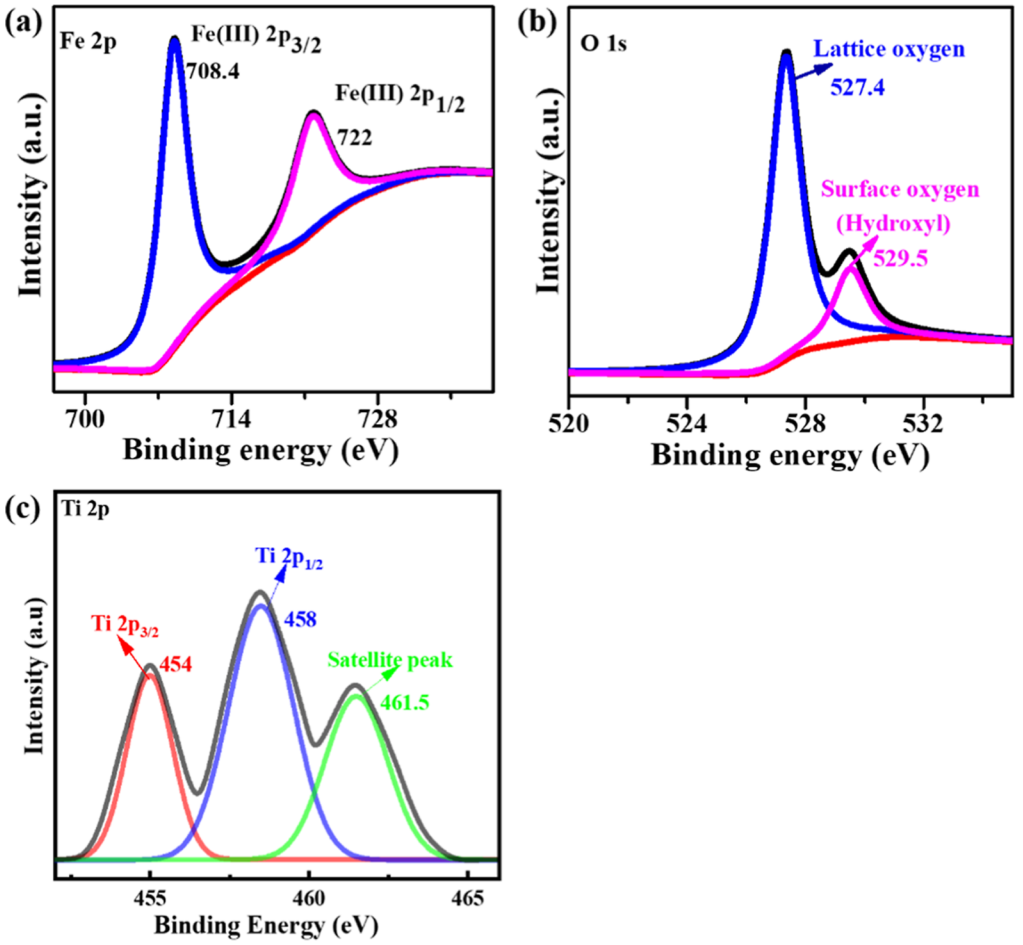

Figure 2. XPS of (a) Fe 2p, (b) O 1s, and (c) Ti 2p.

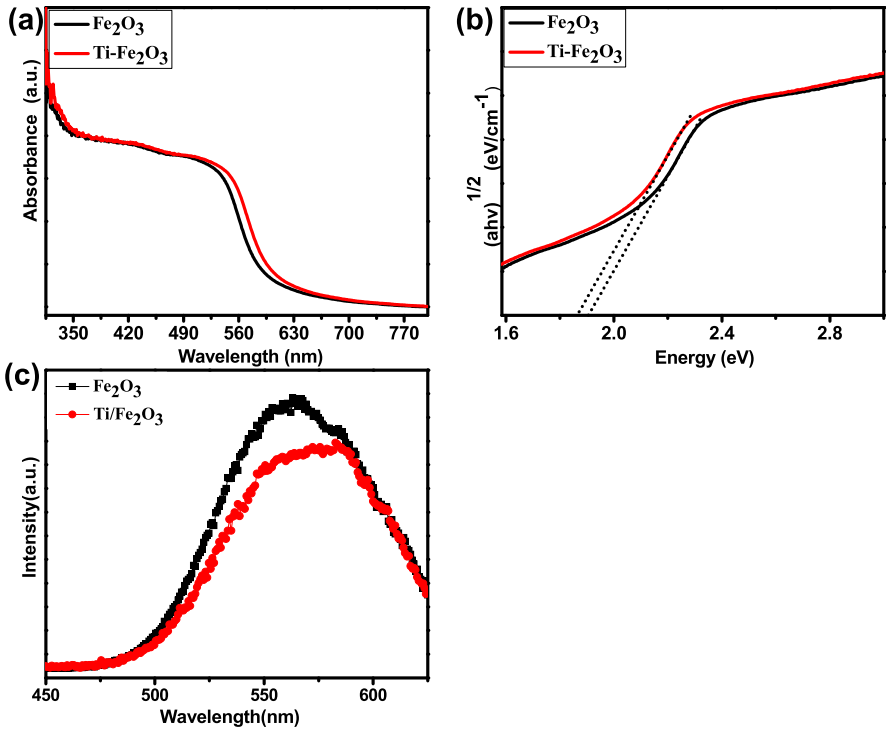

Figure 3. (a) UV−vis diffuse reflectance spectra of Fe_2O_3 and Ti:α-Fe_2O_3 (b) Tauc plot of Fe_2O_3 and Ti:α-Fe_2O_3. (c) Steady-state PL spectra of Fe_2O_3 and Ti:α-Fe_2O_3.

https://doi.org/10.1021/acs.jpcc.5c01995
J. Phys. Chem. C 2025, 129, 13860−13874

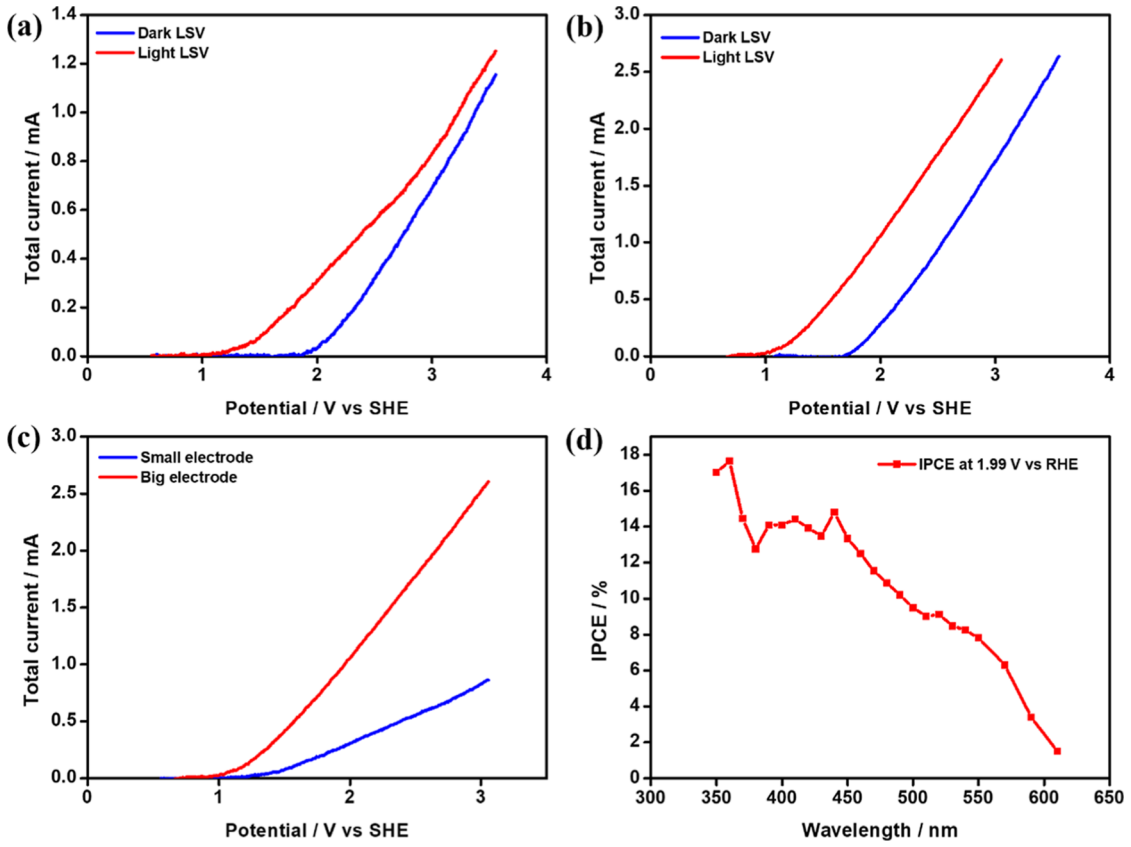

Figure 4. (a) Dark and light LSV comparison for the 1 cm^2 electrode. (b) Dark and light LSV comparison for the 16.8 cm^2 electrode. (c) Comparison between light LSV of the small and big electrode. (d) IPCE recorded with the 1 cm^2 electrode.

substrates, pointing to the large enhancement in charge separation efficiency following Ti(IV) treatment of hematite.[42,43]

3.3. Electrochemical Measurements. For the photoelectrochemical experiments, 1 g/L SDS solutions were prepared. SDS is a salt with a negative charge provided by a sulfonic group and a positive one given by Na^+ counterions. Consequently, SDS works as an intrinsic electrolyte too. However, while the quantity of SDS is significant in mass, its molar concentration is relatively small, around 3.5 mM; it follows that also the ionic strength of the solution is small. Also, the bulky dodecyl-sulfate ion provides relatively low conductivity, around 400 μS.[44,45] The conductivity can be increased by adding an external electrolyte, but this was generally avoided to simulate the use of effluent wastewater having a negligible concentration of other salts. At a second stage, $NaClO_4$ was used as an inert electrolyte to test the impact of increasing the conductivity of the electrolyte on the current/voltage characteristics of the photoanode.

Two Ti:α-Fe_2O_3 electrodes were used, the first one with an area of 1 cm^2 and the second one with an area of 16.8 cm^2. The use of a large area electrode allowing production of a larger current to flow through the cell simplified the detection of gaseous products, whose concentration, according to the Faraday law, scales linearly with the passed charge during the PEC experiments. The voltammetric curves recorded under dark and light conditions are reported in Figure 4. In both cases (large and small electrodes), the generation of photoinduced anodic current anticipating the onset of the dark current of ca. 1 V is evident, showing the transfer of positive carriers to the electrolyte. We note that the larger electrode provides a photocurrent density lowered by ca. a factor of 4 compared to the smaller one. This could be due to limitations arising from the conductivity of the FTO glass and to difficulties in achieving a homogeneous illumination of the whole active area of the photoanode. Nevertheless, the large area electrode still provides a total photocurrent 4 times larger than the small one, making it a better choice for performing gas detection experiments, while the smaller photoanode was mainly exploited to investigate the electrochemical reaction mechanism, being less limited by extrinsic factors like the conductivity of the FTO ohmic support.

The J/V behavior of the 1 cm^2 photoanode in electrolytes 1−4 (see Section 2.4) is reported in Figure 5a. We observe that the highest currents are obtained in $NaClO_4$ containing electrolytes due to their higher conductivity. The presence of organic species, either MeOH or pure SDS, decreases the photocurrent significantly. Overall, the $J/(V\ s)$ are typical for an n-type/electrolyte junction, where the reverse (hole) current generated by holes driven to the interface increases with the positive polarization. However, the photocurrent exhibits a linear rather than exponential increase, typical of systems characterized by a substantial ohmic resistance, in particular in electrolytes 2 and 3. In all cases, the steady-state photocurrent overlaps almost perfectly with that recorded under shuttered mode, showing that the dark current contribution is negligible up to 2.1 V vs RHE, while slow recombination due to surface-accumulated holes contributes to cathodic spikes in the "activation" region of the J/V curve between 1.3 and 1.6 V vs RHE, where the electrochemical potential gradient at the semiconductor-electrolyte junction is still not sufficient to achieve an efficient electron/hole

https://doi.org/10.1021/acs.jpcc.5c01995
J. Phys. Chem. C 2025, 129, 13860−13874

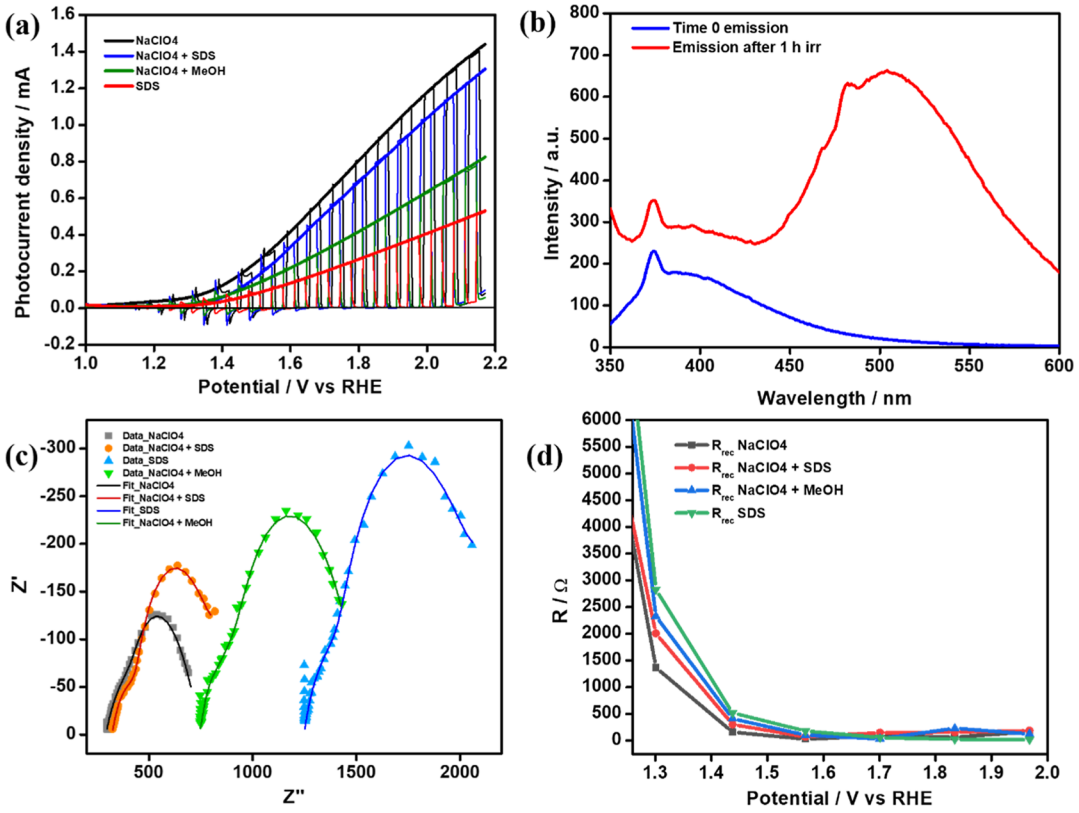

Figure 5. (a) J/V curves of Ti:α-Fe_2O_3 recorded in electrolytes 1−4 under AM 1.5 G illumination. (b) Emission spectrum of a 1 g/L SDS aqueous solution containing 10^{-4} M coumarin, at t_0 (blue plot), and after 1 h of irradiation at 1 sun (100 mW/cm^{-2}), while polarizing the Ti:α-Fe_2O_3 electrode at 2.0 V vs RHE (red plot). (c) Nyquist plot at 1.4 V vs RHE of Ti:α-Fe_2O_3 recorded in electrolytes 1−4 under AM 1.5 G illumination. (d) R_{rec} of Ti:α-Fe_2O_3 recorded in electrolytes 1−4 under AM 1.5 G illumination as a function of the positive bias.

separation. A blank experiment using bare FTO in SDS solution showed no photocurrent at any applied bias potential, Figure S9, thereby confirming that all the observed photocurrent originates from the overlying hematite film.

In order to gain more precise information on the photoelectrochemical behavior of the Ti:α-Fe_2O_3 photoanodes, we performed an incident photon-to-current conversion efficiency (IPCE) analysis in electrolyte 2. The measurement was run at 2.0 V vs RHE, representing a potential very close to that chosen for the SDS degradation experiments. This value was chosen to avoid dark current contribution to the overall circulating current, while having a relevant contribution from the photocurrent. Consistent with the J/V results, the low conductivity of the solution limits the efficiency of the system compared with a highly conductive electrolyte (Figure S5). With SDS, the maximum value of photoconversion is about 18% around 360 nm, Figure 4d. This value decreases to 14% in the blue region (380−450 nm), further dropping to lower percentages (from 10 to 2%) above 470 nm. The resulting shape of the photoconversion efficiency is in good agreement with the typical absorption spectrum of hematite extending down to 600 nm.

3.4. Evidence for OH• Generation. At the anode of the PEC cell, the oxidation of the SDS molecule is expected. A possible route for the total degradation of this pollutant is through radical oxidation mediated by OH•, with the following overall reaction

$$NaSO_4C_{12}H_{25} + 72OH^{\cdot} \rightarrow 12CO_2 + 48H_2O + Na^+ + HSO_4^-$$

It was derived from,[46−48] by adjusting the stoichiometric coefficients to the SDS molecule. In this way, an environmentally impacting molecule like SDS is converted into harmless inorganic species, comprising carbon dioxide and sulfate ions. As described in the next sections, the presence of an excess of CO_2 in the cell atmosphere would prove the ongoing mineralization of the surfactant. OH• radicals for SDS degradation may originate at the photoanode surface from the following reactions

$$H_2O \rightarrow OH^{\cdot} + H^+ + e^-$$

$$OH^- \rightarrow OH^{\cdot} + e^-$$

The first reaction has a potential of E = 2.59 V, while the second one has a potential of 2.02 V, both at pH = 0,[49] and they are both compatible with hematite valence band potential,[50] although additional potential bias is needed to realize cathodic hydrogen evolution, the latter being more negative (on the electrochemical scale) than the hematite flat band potential at pH = 7.

OH• radicals lead to both oxygen evolution and oxidation of SDS molecules. Consequently, at the photoanode, there is generation of oxygen and intermediate products from the OH-mediated SDS oxidation, until mineralization is achieved. The actual presence of hydroxyl radicals, which can induce surfactant degradation, was confirmed by revealing the formation of 7-hydroxy-coumarin as a fluorescent probe.

https://doi.org/10.1021/acs.jpcc.5c01995
J. Phys. Chem. C 2025, 129, 13860−13874

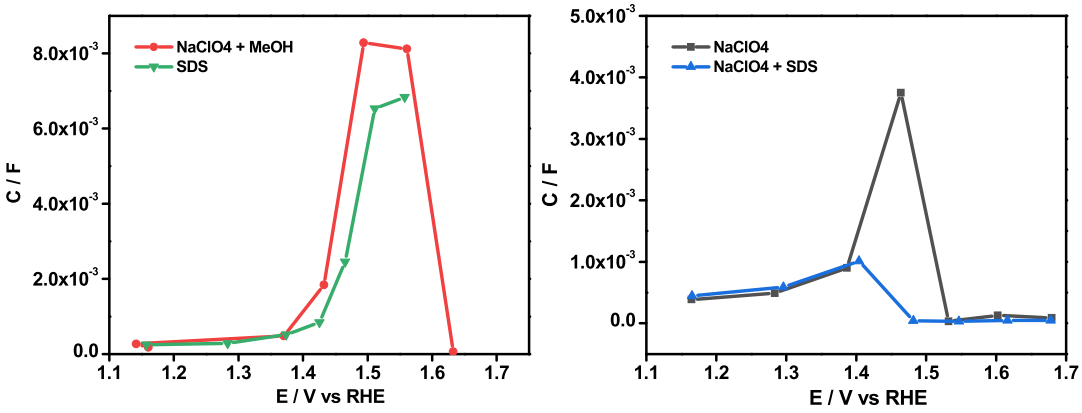

Figure 6. (left) Surface state capacitance (C_{ss}) of Ti:α-Fe_2O_3 in the presence of 1 g/L SDS (green) and of 3.5×10^{-3} M $NaClO_4$ + 3.5×10^{-3} M MeOH (equimolar to SDS). (right) Surface-state capacitance (C_{ss}) of Ti:α-Fe_2O_3 in the presence (blue) and in the absence (black) of 1 g/L SDS. In both cases, the voltage scale was corrected for the iR_S drop according to $V = (V_{app} - iR_S)$, where R_S is the ohmic resistance of the cell.

Under reverse bias and solar simulated illumination, hematite oxidizes water, producing $OH^{\bullet}$ radicals, which, if present, react with coumarin to produce hydroxy-coumarin, which shows an intense emission centered around 500 nm, which is totally lacking in the parent compound, characterized by a weaker emission peaking in the near UV.[51,52] Thus, if $OH^{\bullet}$ radicals are produced at the Ti:α-Fe_2O_3 surface, variations in the emission spectrum of the coumarin containing electrolyte are expected.

We ran a 1 h chronopotentiometry at 2.0 V vs RHE using a Ti:α-Fe_2O_3 photoanode under 1 sun (100 mW/cm^{-2}) irradiation in a solution containing 3.5×10^{-3} M sodium dodecyl sulfate (SDS) and 10^{-4} M coumarin. In order to verify the Ti:α-Fe_2O_3 stability during the experiment, we monitored the photocurrent produced by the electrode as a function of time. The photocurrent density slightly increased during the experiment (Figure S3), proving the stability of the employed substrate. The photocurrent increment is probably due to the presence of reaction intermediates that are easier to oxidize compared with the initial SDS molecule, thus improving interfacial hole scavenging. From Figure 5b, it is possible to observe the characteristic peak of coumarin around 375 nm at t_0 (blue plot). After one hour at 1 sun irradiation, the emission of the hydroxycoumarin was clearly detected, showing without ambiguity the photoelectrochemical generation of hydroxyl radicals during such an experiment.[53] We also observe a raised baseline in the emission spectrum taken after 1 h of irradiation, which affects the whole spectral interval under investigation, but it is particularly evident in the violet/UV blue (350−420 nm), as it should be expected from a light scattering phenomenon. Indeed, we observe the appearance of some cloudiness during the potentiostatic electrolysis, probably due to the formation of less soluble degradation intermediates compared to SDS (Figure S4).

3.5. Electrochemical Impedance Spectroscopy. The representative Nyquist plots taken at 1.4 V vs RHE for electrolytes 1−4 are shown in Figure 5c. Consistent with the J/(V s), we observe the lowest conductivity in the presence of MeOH and SDS. In the presence of SDS alone, the ohmic resistance (the high-frequency intercept of the loop on the real axis) is substantial, being of the order of 1200 Ω. Fits with the electric model of Scheme 2 were generally successful at all the sampled voltages, allowing to reproduce well the J/V behavior of the electrodes, as shown by the correlation of $\sum_i^4 R_i$ with $\frac{\partial V}{\partial I}$ from the J/V curves (Figure S5). R_{rec}, the charge transfer resistance across the interface, largely determines the dependence of the photocurrent delivered by the Ti:α-Fe_2O_3 electrodes on the applied voltage in all of the explored electrolytes and generally decreases with increasing bias in the same fashion as the reciprocal derivative of the J/V does (Figure S5).

From Figure 5d, we observe that the charge-transfer resistance (R_{rec}) in all electrolytes is comparable, indicating that the differences in the J/V behavior in the different electrolytes have to be mainly ascribed to differences in the conductivity of the electrolyte, which also impacts the diffusion of ions within the mesoporous electrodes. The ohmic component (R_S) is potential independent, whereas R_{ct} (bulk charge transport) and W_S (diffusion of ions within the semiconductor) exhibit a moderate dependence on the voltage, generally decreasing with increasing voltage. In general, these latter two are about 1 order of magnitude smaller than R_{rec} in the 1.3−1.5 V vs RHE range but become comparable with R_{rec} past 1.6 V vs RHE. The similarity in the R_{rec} values in all the explored electrolytes is suggestive of the fact that the primary event in all conditions is the hole scavenging by adsorbed water molecules or hydroxylated species at the surface of the semiconductor (i.e., Fe−$(OH)_2$ and/or Fe−OH). This is consistent with the observation of OH radicals as a result of the monoelectronic oxidation of water performed by fluorometric means. The capacitance associated with R_{rec} shows a potential dependence often observed with hematite as a result of hole trapping (which could be in the form of Fe(IV)−O, or Fe(III)−$O^{\bullet}$ intermediates) in surface states below the conduction band edge. We note that in n-type metal oxides, light absorption corresponds to excitation from a valence band with a prevailing pπ oxygen character to a conduction band mainly composed of metal d functions. The transition from delocalized states in the valence band to localized states at the surface corresponds to the hole trapping process. These states act as slow recombination centers, where electrons can be trapped. When the bias is sufficiently strong, surface recombination via surface states is suppressed, and the associated chemical capacitance decreases. This agrees with the observation of recombination transients in the shuttered J/V mode appearing in the potential interval 1.3−1.6 V vs RHE, coincident with the surface capacitance distribution of Figure 6. By comparing the results with $NaClO_4$ in the absence and presence of SDS (electrolytes 1 and 4) we observe that the

https://doi.org/10.1021/acs.jpcc.5c01995
J. Phys. Chem. C 2025, 129, 13860−13874

surface capacitance is decreased with SDS. This effect could be consistent with the following reactions involving hydrated species at the surface of Ti:α-Fe_2O_3. Here, R indicates a generic organic species susceptible to the reaction with reactive oxygen species:

$$Fe(III) - OH + h^+ \rightarrow Fe(III) - O^{\cdot} + H^+ \text{ (hole trapping)} \quad (1)$$

$$Fe(III) - O^{\cdot} + H_2O \rightarrow Fe(III) - OH + {}^{\bullet}OH \text{ (OH radical production)} \quad (2)$$

$$Fe(III) - O^{\cdot} + H^+ + e^- \rightarrow Fe(III) - OH \text{ (recombination via surface states)} \quad (3)$$

$$^{\cdot}OH + {}^{\cdot}OH \rightarrow H_2O_2 \quad (4)$$

$$H_2O_2 + 2h^+ \rightarrow O_2 + 2H^+ \text{ (oxygen evolution)} \quad (5)$$

$$H_2O_2 + {}^{\cdot}OH \rightarrow {}^{\cdot}HO_2 + H_2O \quad (6)$$

$$^{\cdot}HO_2 + H_2O_2 \rightarrow H_2O + O_2 \quad (7)$$

$$Fe(III) - O^{\bullet} + R - H \rightarrow Fe(III) - OH + R^{\bullet} \text{ (formation or organic radicals)} \quad (8)$$

$$^{\cdot}OH + RH \rightarrow R^{\cdot} + H_2O \quad (9)$$

$$R^{\cdot} + O_2 \rightarrow ROO^{\cdot} \text{ (oxidative degradation)} \quad (10)$$

$$2ROO\% \rightarrow 2RO + O_2 \quad (11)$$

Reactions 6 and 7 will proceed in parallel to reaction 5 and will lead to the same product, the organic radical ($R^{\bullet}$) formed as a result of hydrogen abstraction, and are thus virtually indistinguishable, since both involve oxygen radicals which are either surface-bound (hole trapped in surface states) or free to diffuse as $^{\bullet}OH$ radicals. Clearly, freely diffusing $^{\bullet}OH$ radicals can be produced from surface trapped holes according to reaction (2). The presence of an organic scavenger (R) capable of reacting with surface-trapped holes, according to 6, will reduce the density of these intermediates where electrons could no longer be trapped according to reaction (3), causing a drop in C_{ss}. Consistent with this interpretation, the surface capacitance peak is virtually eliminated in the presence of concentrated fast scavengers such as SO_3^{2-} (Figure S6).

Furthermore, we compared the EIS response in the presence of SDS (electrolyte 2) and methanol (electrolyte 3). In the latter case, since no ionic species to ensure conductivity are present, $NaClO_4$ in equimolar amounts to SDS was added. MeOH is a known hole and $OH^{\bullet}$ scavenger for many metal oxide semiconductors, including Ti:α-Fe_2O_3, and allows for a further comparative way to highlight the oxidation mechanism of SDS. We remark here that in the presence of MeOH, ohmic resistance is greatly increased, and a substantial electrode polarization result. Since the flow of electrons out of the photoanode is reduced by the poor cell conductivity, a higher fraction of electrons is trapped in surface states, causing a rise in the surface capacitance peak, which reaches values close to 10 mF.

We observe that, with the voltage correction ($V_{corr} = V_{app} - iR_S$), the surface capacitance distribution of Figure 6left spans a voltage range similar to that in Figure 6right, but the C_{ss} peak is broader since the low conductivity makes the applied bias less effective in promoting charge extraction against surface state recombination. It is also evident that SDS and MeOH afford similar C_{ss} values, but, within the explored voltage range, C_{ss} in the presence of SDS is smaller. This was expected since the SDS molecule, endowed with a long alkyl chain, displays a larger number of sites which, may undergo hydrogen abstraction and hence oxidation compared to MeOH, thus enhancing its scavenging capability. Another reason is the fact that SDS could be partly surface adsorbed at the Ti:α-Fe_2O_3 interface, again resulting in an improved scavenging of surface-trapped holes with respect to MeOH. This is consistent with the observation that at certain voltages and at low frequencies an inductive loop appeared (Figure S7), which has been ascribed by some authors to a phase shift in the impedance caused by adsorbed intermediates.[54−56] However, in the present treatment, for the sake of generality, we did not include the inductor in our electrical model, since only at certain voltages and with SDS-based electrolytes was this elusive feature clearly observed. Furthermore, inclusion of the inductor did not cause substantial deviations from the resistance and capacitance values extracted from the fits.

SDS tendency to absorb onto the hematite surface has also been evidenced by Cyclic Voltammetry analyses in dark conditions conducted in electrolyte 1 (3.5×10^{-3} M $NaClO_4$) and electrolyte 4 (3.5×10^{-3} M $NaClO_4$ and 3.5×10^{-3} M SDS) to address the electrochemical response of the electrode−electrolyte interface in the presence and absence of this tensioactive species (Figure S12). The CVs were recorded from −0.4 V to +1.2 V vs SCE, scanning the potential first in the anodic and then in the cathodic direction, and then reversed, to observe if dynamics dependent on the polarization direction were present. In the presence of $NaClO_4$ only (blue curve), all of the scans are perfectly overlapping, regardless of whether the scan starts from the cathodic or anodic direction. In the presence of SDS, however, a change is observed during the first scan (black and purple curves); the onset of the reductive wave can already be seen at potentials slightly below zero. From the second scan onward, the curve gradually approaches the blue one recorded in $NaClO_4$ alone until it almost completely overlaps the latter starting from the third scan. This suggests that SDS effectively adsorbs on the electrode surface, affecting the energy and the density of surface states close to the conduction band edge, and as potential scans are repeated, the surfactant is progressively removed from the electrode surface, restoring the usual electrochemical response we observe in $NaClO_4$.

Figure S13a shows the photopotential decay profile over time of a Ti/Fe_2O_3 photoanode in electrolytes 1 and 4. In the presence of SDS (red curve), the photopotential exhibits a faster decay compared to $NaClO_4$ alone (blue curve), although, in general, due to poor conductivity, the photovoltage decay is extremely slow. Moreover, we calculated the electron lifetime using the following formula[57]

$$\tau = -\frac{kT}{e}\left(\frac{dV_{oc}}{dt}\right)^{-1}$$

In general, from Figure S13b it is possible to observe that the electron lifetime increases as the potential becomes more

https://doi.org/10.1021/acs.jpcc.5c01995
J. Phys. Chem. C 2025, 129, 13860−13874

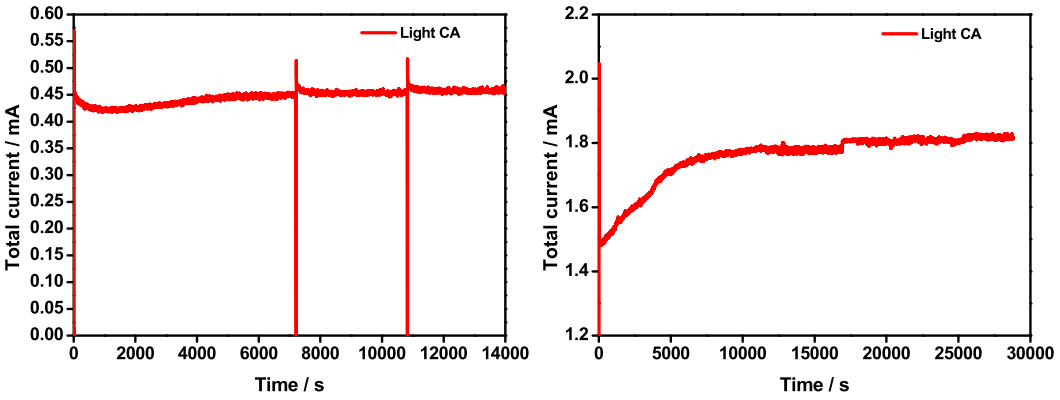

Figure 7. (left) Light CA run with a small electrode at 2.15 V vs RHE of applied bias. (right) Light CA run with a big electrode at 2.15 V vs RHE of applied bias.

positive, spanning ca. 3 orders of magnitude in the s time scale. In the presence of SDS, the decay is faster, likely due to an additional recombination pathway, which may involve partially oxidized SDS adsorbed at the hematite electrode.

3.6. Hydrogen Evolution. From LSV curves, Figure 3, at the potential of 2.15 V vs RHE, there is the maximum difference between current under illumination and dark current. For this reason, this value has been chosen for running a CA in order to study the degradation of the surfactant and the hydrogen production yield. The selected voltage was applied to the cell for a maximum of 5.5 h, during which gas chromatographic runs were acquired at constant intervals of about 3 min, which is the time required by the machine to complete a measurement. Among all the acquired chromatograms, 10 were chosen for a quantitative analysis: the first five were the ones acquired just before starting the experiment, while the second five were obtained in a steady-state situation (according to photocurrent data).

From Figure S9, for example, it can be observed that a dark electrode made of SnO_2, which is considered to be a good metal oxide for electrochemical incineration processes, does not produce any sizable current in our experimental conditions out to about 2.2 V vs RHE. Under these conditions, the hematite electrode already produces a current of ca. 1 mA/cm^2, which is translated into hydrogen evolving at the counter electrode of the cell. In this sense, compared to a dark electrochemical system, the solar assisted process allows a net (positive) saving in energy that can be quantified by directly measuring the amount of produced hydrogen produced in the cell compared to the dark experiments.

In the small electrode case, the 2.15 V potential was applied for about 4 h, obtaining the result in Figure 7left below.

As one can see from the CA data, about 12,000 s after the beginning of the experiment, there is a plateau in the current value. This point was then recognized as a steady-state regime, and the corresponding chromatograms, which are the ones acquired in that period, are used to estimate the hydrogen and carbon dioxide concentrations, Figure S8a,c. In particular, Figure S8a shows the hydrogen GC curves acquired in three different regimes. At the beginning of the blue curve, there is no hydrogen in the cell atmosphere; therefore, the curve is flat. In the steady-state situation, the production of hydrogen is higher because of the water reduction reaction at the cathode (red curve). Finally, 1 h after switching off current, the peak is much smaller because the production of hydrogen stopped (green curve), and the atmosphere was constantly cleaned by the nitrogen flux. This result confirms the ongoing water reduction at the cathode of the cell.

The same pattern is visible in the picture on the right, which refers to the carbon dioxide case. In the steady-state regime, the CO_2 peak is bigger than both those before and after the experiment. Because carbon dioxide is the final compound in the SDS degradation chain, its presence in the cell while current is circulating is strong proof that, at the photoanode, mineralization of this pollutant is proceeding and, as a consequence, water remediation is taking place. By exploiting the calibration of the GC instrument, it is possible to quantify CO_2 and H_2 during the peculiar stages of the experiment, whose results are shown in Table 1. In fact, the area of each chromatographic peak is linearly proportional to the concentration of that specific gas in the incoming mixture.

Table 1. Hydrogen and Carbon Dioxide Concentration before and in the Steady-State Regime of SDS Degradation with Small and Big Electrodes

small electrode	H_2 [ppm]	CO_2 [ppm]
before	2 ± 4	10 ± 2
steady-state	173 ± 12	21 ± 3
big electrode	H_2 [ppm]	CO_2 [ppm]
before	7 ± 4	21 ± 3
steady-state	830 ± 60	66 ± 5

The same experiments were repeated for the large area Ti:α-Fe_2O_3 electrode. This time, the chronoamperometry was run for 8 h, Figure 7right above. In this case, a suitably stable regime is found after about 20,000 s, and the acquired curves show the following behavior.

Even in this case, there is a much higher concentration of hydrogen and carbon dioxide after 20,000 s than at the beginning of the experiment, Figure S8b,d and Table 1. After the current is switched off, the CO_2 concentration remains pretty high, probably because of retention inside the cell. This aspect has not been further investigated because it is of less scientific interest with respect to the transition from starting point to the steady-state regime. The concentration of H_2 in the steady-state regime is almost 5 times larger than that in the small electrode case, thus reflecting the 4-fold larger current that circulates in the PEC.

The rate at which hydrogen is produced can be estimated in 2 ways. The first one is by integrating electrical current data over time in order to find the total number of electrons that

https://doi.org/10.1021/acs.jpcc.5c01995
J. Phys. Chem. C 2025, 129, 13860−13874

have been exchanged in a unit of time. By knowing that the synthesis of a hydrogen molecule requires 2 electrons, it is then possible to find the rate of production. The other way is from GC measurements: by knowing the value at which nitrogen is fluxed in the reactor and by assuming both ideal gas conditions and no trapping of the carrier gas by the liquid, it is possible to determine the rate from the measured concentration throughout this formula

$$R_{H_2} = 60\varphi[H_2]/V_{mol} \quad (3)$$

where 60 indicates the number of minutes in 1 h, φ = 10 sccm is the nitrogen flux, $[H_2]$ is the measured hydrogen concentration, and V_{mol} = 22,400 cc is the volume occupied by a mole of gas, assuming ideal conditions. Actually, the outcoming flux is a little bit larger than 10 sccm because of the water evaporation. But from knowing the water vapor tension at this temperature, this effect should account for 2−3% of the overall flux. Consequently, the H_2 production rate is underestimated, but the error is within the accuracy with which the concentrations are measured from the GC curves. In the small electrode case, a rate of $R = 8.54 \pm 0.03$ μmol/h has been found from electrical current data, while a rate of $R = 4.6 \pm 0.3$ μmol/h has been estimated from GC measurements. The discrepancy (a factor of ca. 1.8) between the two results may be explained by considering that, from electrical current data, it is assumed that all electrons are employed in the hydrogen evolution reaction (HER), whereas in reality, in a single compartment cell, other competitive reactions may occur at the cathode, including reduction of SDS oxidation intermediates and, particularly, of molecular oxygen evolved at the anode.

The same comparison can be done for the large area electrode, obtaining $R = 33.65 \pm 0.03$ μmol/h from electrical current and $R = 22 \pm 2$ μmol/h from GC measurements, affording a ratio of 1.5, which is quite comparable to the previous case, pointing to the presence of the same competitive reactions explained before occurring with comparable efficiency. In this case, consistent with the Faraday laws, the rate of hydrogen production is about 4 times larger than that in the small electrode case.

In order to have an estimation of the contribution of photons toward hydrogen generation, we employ a power-saving parameter, η, which is defined as follows

$$\eta = \Phi \times Q/P/A \quad (4)$$

where Φ is the hydrogen production rate difference between light and dark conditions at the same applied voltage, expressed in mmol/s, Q is the hydrogen formation energy, 237 kJ/mol, P is the illumination power, 100 mW/cm^2, while A is the illuminated electrode area, measured in cm^2. This figure of merit should be understood as the gain in hydrogen production over a dark experiment performed with the same electrode at the same voltage. The chosen bias, 2.15 V, is just before the dark current onset and represents the maximum voltage that can be applied under dark conditions before non-negligible H_2 production starts.

In this work, for the small electrode, the power saving was η = 0.3%, while for the bigger one, it was equal to η = 0.13%. The smaller efficiency in the big electrode case with respect to the small one reflects the smaller current density at the same applied bias. Moreover, these values are far smaller than the ideal one, but this work represents a proof-of-concept study of the possibility of achieving solar hydrogen production from surfactant-rich wastewaters. There are then many factors that limit the achievable efficiency, like the very small molar concentration of the solution or geometrical factors in the case of the large area electrode.

4. CONCLUSIONS

We investigated here a strategy for PEC solar hydrogen production starting from SDS-rich wastewater. This surfactant is of wide use in industrial and domestic applications, and this is the reason why its presence is relevant in wastewater. However, it is also potentially suitable as a hole scavenger to enhance hydrogen production. A titanium-doped hematite photoanode was employed as the working electrode. Here, Ti doping was proven to be very effective in increasing photocurrent at moderately small overpotentials by reducing both bandgap and charge recombination of the photoanode. The oxidation of SDS, which acts as a hole scavenger at the anode surface, proceeds by means of radical oxidation. Fluorescence experiments allowed us to confirm the oxidation mechanism, which involves water oxidation to OH$^\bullet$ radicals, which then attack SDS, degrading the apolar carbon tail of the surfactant and converting it into CO_2. EIS enlightened the charge transfer dynamics of the PEC system, whose behavior has been analyzed in four different electrolytes. In particular, the selectivity of the system toward the oxidation of SDS rather than the degradation of a sacrificial species (MeOH in this case) is likely due to a partial adsorption of the surfactant on the surface of the photoanodes, which leads to an improved scavenging of surface-trapped holes with respect to MeOH. Both the goals of the cell have been confirmed by GC, which revealed hydrogen gas and carbon dioxide, the latter proving the mineralization of the surfactant. Thanks to this analysis, power saving efficiencies for the systems have been calculated, resulting in η = 0.13% for the big electrode and η = 0.3% for the smaller one. These values are far from ideal, and further studies are needed to optimize the reaction conditions and parameters in order to increase the efficiency of the system. Nevertheless, this research provides a proof-of-concept demonstration of the possibility of producing solar H_2 by using surfactant-rich wastewaters as the substrate instead of fresh water, thus providing wastewater remediation and a simultaneous waste valorization. In fact, our system has shown long and sustained H_2 production without the addition of any electrolyte and without any pH adjustment. This provides a critical advancement toward the scalability of this application. Despite a large cell resistance, confirmed by EIS measurement, our H_2 production rates are compatible with the literature results for similar systems. Additionally, this work also provides an in-depth analysis of the photoanodic reaction mechanisms, providing a step beyond the current understanding of photoelectrochemical reactions and a convenient starting point for further optimization studies.

■ ASSOCIATED CONTENT

Supporting Information

The Supporting Information is available free of charge at https://pubs.acs.org/doi/10.1021/acs.jpcc.5c01995.

GC calibration; additional PEC and EIS measurements, and GC curves (PDF)

https://doi.org/10.1021/acs.jpcc.5c01995
J. Phys. Chem. C 2025, 129, 13860−13874

AUTHOR INFORMATION

Corresponding Authors

Silvia Grandi − *Department of Chemical, Pharmaceutical and Agricultural Sciences, University of Ferrara, 44121 Ferrara, Italy*; Email: silvia.grandi@unife.it

Michele Orlandi − *Physics Department, University of Trento, 38123 Povo, Trento, Italy*; orcid.org/0000-0001-5738-3231; Email: michele.orlandi@unitn.it

Authors

Alessandro Chesini − *Physics Department, University of Trento, 38123 Povo, Trento, Italy*

Stefano Caramori − *Department of Chemical, Pharmaceutical and Agricultural Sciences, University of Ferrara, 44121 Ferrara, Italy; National Interuniversity Consortium of Materials Science and Technology (INSTM), University of Ferrara Research Unit, 44121 Ferrara, Italy*

Michele Mazzanti − *Department of Chemical, Pharmaceutical and Agricultural Sciences, University of Ferrara, 44121 Ferrara, Italy*

Luca Matteo Martini − *Physics Department, University of Trento, 38123 Povo, Trento, Italy*; orcid.org/0000-0002-4501-3492

Khakemin Khan − *Physics Department, University of Trento, 38123 Povo, Trento, Italy*

Antonio Miotello − *Physics Department, University of Trento, 38123 Povo, Trento, Italy*

Complete contact information is available at: https://pubs.acs.org/10.1021/acs.jpcc.5c01995

Author Contributions

Alessandro Chesini: writing—original draft, investigation, and formal analysis. **Silvia Grandi:** writing—original draft, investigation, and formal analysis. **Stefano Caramori:** writing—review and editing, conceptualization, methodology, and supervision. **Michele Mazzanti:** investigation and formal analysis. **Luca Matteo Martini:** methodology and writing—review and editing. **Khakemin Khan:** investigation and writing—review and editing **Michele Orlandi:** writing—review and editing, supervision, methodology, and conceptualization. **Antonio Miotello:** writing—review and editing and funding acquisition.

Notes

The authors declare no competing financial interest.

ACKNOWLEDGMENTS

The authors acknowledge Dr. Nicola Bazzanella and Claudio Cestari for technical help. This work was supported by project "Produrre Idrogeno in Trentino—H2@TN" (PAT-Trento). Silvia Grandi would like to acknowledge financial support from the Emilia Romagna Region (PNRR, D.M. 1061/2021) as well as from the PRIN−PNRR MUR project "Leaf" (Prot. P20229L2EE).

REFERENCES

(1) IRENA. *Renewable Capacity Statistics 2024*: Abu Dabhi, 2024.

(2) Yang, Y.; Bremner, S.; Menictas, C.; Kay, M. Modelling and Optimal Energy Management for Battery Energy Storage Systems in Renewable Energy Systems: A Review. *Renewable Sustainable Energy Rev.* **2022**, *167*, 112671.

(3) Burton, N. A.; Padilla, R. V.; Rose, A.; Habibullah, H. Increasing the Efficiency of Hydrogen Production from Solar Powered Water Electrolysis. *Renewable Sustainable Energy Rev.* **2021**, *135*, 110255.

(4) Mazloomi, K.; Gomes, C. Hydrogen as an Energy Carrier: Prospects and Challenges. *Renewable Sustainable Energy Rev.* **2012**, *16* (5), 3024−3033.

(5) Wang, M.; Wang, Z.; Gong, X.; Guo, Z. The Intensification Technologies to Water Electrolysis for Hydrogen Production − A Review. *Renewable Sustainable Energy Rev.* **2014**, *29*, 573−588.

(6) Kélouwani, S.; Agbossou, K.; Chahine, R. Model for Energy Conversion in Renewable Energy System with Hydrogen Storage. *J. Power Sources* **2005**, *140* (2), 392−399.

(7) Forsythe, R. C.; Müller, A. M. Quo Vadis Water Oxidation? *Catal. Today* **2022**, *388*−*389*, 329−332.

(8) Orlandi, M.; Mazzi, A.; Arban, G.; Bazzanella, N.; Rudatis, P.; Caramori, S.; Patel, N.; Fernandes, R.; Bignozzi, C. A.; Miotello, A. On the Effect of Sn-Doping in Hematite Anodes for Oxygen Evolution. *Electrochim. Acta* **2016**, *214*, 345−353.

(9) Dalle Carbonare, N.; Carli, S.; Argazzi, R.; Orlandi, M.; Bazzanella, N.; Miotello, A.; Caramori, S.; Bignozzi, C. A. Improvement of the Electron Collection Efficiency in Porous Hematite Using a Thin Iron Oxide Underlayer: Towards Efficient All-Iron Based Photoelectrodes. *Phys. Chem. Chem. Phys.* **2015**, *17* (44), 29661−29670.

(10) Zhao, S.; Liu, B.; Zhang, G.; Wang, Q.; Cai, Y.; Tong, Y.; Wang, S.; Zhang, P.; Wang, T.; Gong, J. Sputtered Stainless Steel on Silicon Photoanode for Stable Seawater Splitting in Photoelectrochemical Flow Cell. *Trans. Tianjin Univ.* **2023**, *29* (6), 473−481.

(11) Dingenen, F.; Verbruggen, S. W. Tapping Hydrogen Fuel from the Ocean: A Review on Photocatalytic, Photoelectrochemical and Electrolytic Splitting of Seawater. *Renewable Sustainable Energy Rev.* **2021**, *142*, 110866.

(12) Cristino, V.; Pasti, L.; Marchetti, N.; Berardi, S.; Bignozzi, C. A.; Molinari, A.; Passabi, F.; Caramori, S.; Amidani, L.; Orlandi.; et al. Photoelectrocatalytic Degradation of Emerging Contaminants at WO3/BiVO4 Photoanodes in Aqueous Solution. *Photochem. Photobiol. Sci.* **2019**, *18* (9), 2150−2163.

(13) Davies, K. R.; Allan, M. G.; Nagarajan, S.; Townsend, R.; Dunlop, T.; McGettrick, J. D.; Asokan, V. S.; Ananthraj, S.; Watson, T.; Godfrey.; et al. S. Solar Light-Driven Simultaneous Pharmaceutical Pollutant Degradation and Green Hydrogen Production Using a Mesoporous Nanoscale WO3/BiVO4 Heterostructure Photoanode. *J. Environ. Chem. Eng.* **2023**, *11* (3), 110256.

(14) Rioja-Cabanillas, A.; McMichael, S.; Tolosana-Moranchel, A.; Alkharabsheh, S.; Skillen, N.; Fernandez-Ibañez, P.; Byrne, J. A. Solar Photoelectrocatalytic Oxidation of Urea in Water Coupled to Green Hydrogen Production. *J. Cleaner Prod.* **2023**, *419*, 138200.

(15) Shen, Z.; Li, J.; Zhang, Y.; Bai, J.; Tan, X.; Li, X.; Qiao, L.; Xu, Q.; Zhou, B. Highly Efficient Total Nitrogen and Simultaneous Total Organic Carbon Removal for Urine Based on the Photoelectrochemical Cycle Reaction of Chlorine and Hydroxyl Radicals. *Electrochim. Acta* **2019**, *297*, 1−9.

(16) Verlicchi, P.; Al Aukidy, M.; Zambello, E. Occurrence of Pharmaceutical Compounds in Urban Wastewater: Removal, Mass Load and Environmental Risk after a Secondary Treatment—A Review. *Sci. Total Environ.* **2012**, *429*, 123−155.

(17) Siyal, A. A.; Shamsuddin, M. R.; Low, A.; Rabat, N. E. A Review on Recent Developments in the Adsorption of Surfactants from Wastewater. *J. Environ. Manage.* **2020**, *254*, 109797.

(18) Orlandi, M.; Filosa, N.; Bettonte, M.; Fendrich, M.; Girardini, M.; Battistini, T.; Miotello, A. Treatment of Surfactant-Rich Industrial Wastewaters with Concentrated Sunlight: Toward Solar Wastewater Remediation. *Int. J. Environ. Sci. Technol.* **2019**, *16* (4), 2109−2114.

(19) Jaramillo-Gutiérrez, M. I.; Aparicio-Mauricio, G.; Pedraza-Avella, J. A.; Rivero, E. P.; Cruz-Díaz, M. R. Indirect Oxidation of an Anionic Surfactant Presents in Produced Water in a Tubular Photoelectrochemical Reactor with Concentric Expanded Meshes: Experimental Study and Mathematical Modeling. *Electrochim. Acta* **2025**, *517*, 145721.

(20) Badmus, S. O.; Amusa, H. K.; Oyehan, T. A.; Saleh, T. A. Environmental Risks and Toxicity of Surfactants: Overview of

Analysis, Assessment, and Remediation Techniques. *Environ. Sci. Pollut. Res.* **2021**, *28* (44), 62085−62104.
(21) Adak, A.; Bandyopadhyay, M.; Pal, A. Removal of Anionic Surfactant from Wastewater by Alumina: A Case Study. *Colloids Surf., A* **2005**, *254* (1), 165−171.
(22) Zheng, Z.; He, J.; Man, J. H. K.; Dong, T.; Lo, I. M. C. Hydrogen Production from Photoelectrochemical Wastewater Treatment: Advancing toward Sustainability. *Curr. Opin. Chem. Eng.* **2025**, *47*, 101096.
(23) Torres-Pinto, A.; Díez, A. M.; Silva, C. G.; Faria, J. L.; Sanromán, M. A.; Silva, A. M. T.; Pazos, M. Photoelectrocatalytic Degradation of Pharmaceuticals Promoted by a Metal-Free G-C3N4 Catalyst. *Chem. Eng. J.* **2023**, *476*, 146761.
(24) Dang, Q.; Wang, L.; Liu, J.; Wang, D.; Chai, J.; Wu, M.; Tang, L. Recent Progress of Photoelectrocatalysis Systems for Wastewater Treatment. *J. Water Proc. Eng.* **2023**, *53*, 103609.
(25) Groenen Serrano, K. Chapter 6 - Indirect Electrochemical Oxidation Using Hydroxyl Radical, Active Chlorine, and Peroxodisulfate. In *Electrochemical Water and Wastewater Treatment*; Martínez-Huitle, C. A., Rodrigo, M. A., Scialdone, O., Eds.; Butterworth-Heinemann, 2018; pp 133−164..
(26) Berardi, S.; Cristino, V.; Bignozzi, C. A.; Grandi, S.; Caramori, S. Hematite-Based Photoelectrochemical Interfaces for Solar Fuel Production. *Inorg. Chim. Acta* **2022**, *535*, 120862.
(27) Mazzaro, R.; Boscolo Bibi, S.; Natali, M.; Bergamini, G.; Morandi, V.; Ceroni, P.; Vomiero, A. Hematite Nanostructures: An Old Material for a New Story. Simultaneous Photoelectrochemical Oxidation of Benzylamine and Hydrogen Production through Ti Doping. *Nano Energy* **2019**, *61*, 36−46.
(28) Piccioni, A.; Vecchi, P.; Vecchi, L.; Grandi, S.; Caramori, S.; Mazzaro, R.; Pasquini, L. Distribution of Relaxation Times Based on Lasso Regression: A Tool for High-Resolution Analysis of IMPS Data in Photoelectrochemical Systems. *J. Phys. Chem. C* **2023**, *127* (17), 7957−7964.
(29) Bora, D. K. Fabrication of Silicon Doped Hematite Photoelectrode with Enhanced Photocurrent Density via Solution Processing of an In-Situ TEOS Modified Precursor. *Mater. Sci. Semicond. Process.* **2015**, *31*, 728−738.
(30) Sivula, K.; Zboril, R.; Le Formal, F.; Robert, R.; Weidenkaff, A.; Tucek, J.; Frydrych, J.; Grätzel, M. Photoelectrochemical Water Splitting with Mesoporous Hematite Prepared by a Solution-Based Colloidal Approach. *J. Am. Chem. Soc.* **2010**, *132* (21), 7436−7444.
(31) Carrai, I.; Mazzaro, R.; Bassan, E.; Morselli, G.; Piccioni, A.; Grandi, S.; Caramori, S.; Ceroni, P.; Pasquini, L. Photoelectrochemical Valorization of Biomass Derivatives with Hematite Photoanodes Modified by Cocatalysts. *Sol. RRL* **2023**, *7* (16), 2300205.
(32) Dias, P.; Andrade, L.; Mendes, A. Hematite-Based Photoelectrode for Solar Water Splitting with Very High Photovoltage. *Nano Energy* **2017**, *38*, 218−231.
(33) Hirschorn, B.; Orazem, M. E.; Tribollet, B.; Vivier, V.; Frateur, I.; Musiani, M. Determination of Effective Capacitance and Film Thickness from Constant-Phase-Element Parameters. *Electrochim. Acta* **2010**, *55* (21), 6218−6227.
(34) Taylor, S. R.; Gileadi, E. Physical Interpretation of the Warburg Impedance. *Corrosion* **1995**, *51* (9), 664−671.
(35) Carrai, I.; Mazzaro, R.; Bellatreccia, C.; Piccioni, A.; Salvi, M.; Grandi, S.; Caramori, S.; Ceroni, P.; Pasquini, L. Nickel-Based Cocatalysts on Titanium-Doped Hematite Empower Direct Photoelectrochemical Valorisation of 5-Hydroxymethylfurfural. *ChemSusChem* **2025**, *18* (9), No. e202402604.
(36) Bhargava, G.; Gouzman, I.; Chun, C. M.; Ramanarayanan, T. A.; Bernasek, S. L. Characterization of the "Native" Surface Thin Film on Pure Polycrystalline Iron: A High Resolution XPS and TEM Study. *Appl. Surf. Sci.* **2007**, *253* (9), 4322−4329.
(37) Sheel, D. W.; Lewis, J.; Robinson, A.; Yates, H. M. Doped Iron Oxide Thin Films for Photoelectrochemical Generation of Hydrogen from Water. *ECS Meet. Abstr.* **2009**, *MA2009-02* (34), 2633.
(38) Dhananjeyan, M. R.; Mielczarski, E.; Thampi, K. R.; Buffat, Ph.; Bensimon, M.; Kulik, A.; Mielczarski, J.; Kiwi, J. Photodynamics and Surface Characterization of TiO2 and Fe2O3 Photocatalysts Immobilized on Modified Polyethylene Films. *J. Phys. Chem. B* **2001**, *105* (48), 12046−12055.
(39) Greczynski, G.; Haasch, R. T.; Hellgren, N.; Lewin, E.; Hultman, L. X-Ray Photoelectron Spectroscopy of Thin Films. *Nat. Rev. Methods Primers* **2023**, *3* (1), 41.
(40) Chen, X.; Liu, L.; Yu, P. Y.; Mao, S. S. Increasing Solar Absorption for Photocatalysis with Black Hydrogenated Titanium Dioxide Nanocrystals. *Science* **2011**, *331* (6018), 746−750.
(41) Jiang, D.; Otitoju, T. A.; Ouyang, Y.; Shoparwe, N. F.; Wang, S.; Zhang, A.; Li, S. A Review on Metal Ions Modified TiO2 for Photocatalytic Degradation of Organic Pollutants. *Catalysts* **2021**, *11* (9), 1039.
(42) Berardi, S.; Kopula Kesavan, J.; Amidani, L.; Meloni, E. M.; Marelli, M.; Boscherini, F.; Caramori, S.; Pasquini, L. Better Together: Ilmenite/Hematite Junctions for Photoelectrochemical Water Oxidation. *ACS Appl. Mater. Interfaces* **2020**, *12* (42), 47435−47446.
(43) Carrai, I.; Mazzaro, R.; Bassan, E.; Morselli, G.; Piccioni, A.; Grandi, S.; Caramori, S.; Ceroni, P.; Pasquini, L. Photoelectrochemical Valorization of Biomass Derivatives with Hematite Photoanodes Modified by Cocatalysts. *Sol. RRL* **2023**, *7* (16), 2300205.
(44) Mateus, M.; Araújo, L.; Leopoldino, A.; Ferreira, M.; Ferreira, D.; Luz, M.; Gonçalves, J. Molecular Interactions and Modeling of Anionic Surfactant Effect on Oxygen Transfer in a Cylindrical Reactor. *Environ. Eng. Sci.* **2019**, *36*, 180−185.
(45) Al-Soufi, W.; Piñeiro, L.; Novo, M. A Model for Monomer and Micellar Concentrations in Surfactant Solutions: Application to Conductivity, NMR, Diffusion, and Surface Tension Data. *J. Colloid Interface Sci.* **2012**, *370*, 102−110.
(46) Sires, I.; Brillas, E.; Oturan, M. A.; Rodrigo, M. A.; Panizza, M. Electrochemical Advanced Oxidation Processes: Today and Tomorrow. A Review. *Environ. Sci. Pollut. Res.* **2014**, *21* (14), 8336−8367.
(47) Panizza, M.; Delucchi, M.; Cerisola, G. Electrochemical Degradation of Anionic Surfactants. *J. Appl. Electrochem.* **2005**, *35* (4), 357−361.
(48) dos Santos, A. J.; Shen, H.; Lanza, M. R. V.; Li, Q.; Garcia-Segura, S. Electrochemical Oxidation of Surfactants as an Essential Step to Enable Greywater Reuse. *Environ. Technol. Innovation* **2024**, *34*, 103563.
(49) Koppenol, W. H.; Liebman, J. F. The Oxidizing Nature of the Hydroxyl Radical. A Comparison with the Ferryl Ion (FeO2+). *J. Phys. Chem.* **1984**, *88* (1), 99−101.
(50) Bassi, P. S.; Gurudayal; Wong, L. H.; Barber, J. Iron Based Photoanodes for Solar Fuel Production. *Phys. Chem. Chem. Phys.* **2014**, *16* (24), 11834−11842.
(51) Wafi, A.; Szabó-Bárdos, E.; Horváth, O.; Makó, E.; Jakab, M.; Zsirka, B. Coumarin-Based Quantification of Hydroxyl Radicals and Other Reactive Species Generated on Excited Nitrogen-Doped TiO2. *J. Photochem. Photobiol., A* **2021**, *404*, 112913.
(52) Cristino, V.; Marinello, S.; Molinari, A.; Caramori, S.; Carli, S.; Boaretto, R.; Argazzi, R.; Meda, L.; Bignozzi, C. A. Some Aspects of the Charge Transfer Dynamics in Nanostructured WO3 Films. *J. Mater. Chem. A* **2016**, *4* (8), 2995−3006.
(53) Leandri, V.; Gardner, J. M.; Jonsson, M. Coumarin as a Quantitative Probe for Hydroxyl Radical Formation in Heterogeneous Photocatalysis. *J. Phys. Chem. C* **2019**, *123* (11), 6667−6674.
(54) Dunn, H. K.; Feckl, J. M.; Müller, A.; Fattakhova-Rohlfing, D.; Morehead, S. G.; Roos, J.; Peter, L. M.; Scheu, C.; Bein, T. Tin Doping Speeds up Hole Transfer during Light-Driven Water Oxidation at Hematite Photoanodes. *Phys. Chem. Chem. Phys.* **2014**, *16* (44), 24610−24620.
(55) Müller, J. T.; Urban, P. M.; Hölderich, W. F. Impedance Studies on Direct Methanol Fuel Cell Anodes. *J. Power Sources* **1999**, *84* (2), 157−160.
(56) Harrington, D. A.; Conway, B. E. Ac Impedance of Faradaic Reactions Involving Electrosorbed Intermediates—I. Kinetic Theory. *Electrochim. Acta* **1987**, *32* (12), 1703−1712.

https://doi.org/10.1021/acs.jpcc.5c01995
J. Phys. Chem. C 2025, 129, 13860−13874

(57) Zaban, A.; Greenshtein, M.; Bisquert, J. Determination of the Electron Lifetime in Nanocrystalline Dye Solar Cells by Open-Circuit Voltage Decay Measurements. *ChemPhysChem* **2003**, *4* (8), 859−864.

https://doi.org/10.1021/acs.jpcc.5c01995
J. Phys. Chem. C 2025, 129, 13860−13874